Design and Batch Fabrication of Probes for Sub-100 nm Scanning Thermal Microscopy

Li Shi, Ohmyoung Kwon, Andrew C. Miner, and Arunava Majumdar

***Abstract*—A batch fabrication process has been developed for making cantilever probes for scanning thermal microscopy (SThM) with spatial resolution in the sub-100 nm range. A heat transfer model was developed to optimize the thermal design of the probes. Low thermal conductivity silicon dioxide and silicon nitride were chosen for fabricating the probe tips and cantilevers, respectively, in order to minimize heat loss from the sample to the probe and to improve temperature measurement accuracy and spatial resolution. An etch process was developed for making silicon dioxide tips with tip radius as small as 20 nm. A thin film thermocouple junction was fabricated at the tip end with a junction height that could be controlled in the range of 100–600 nm. These thermal probes have been used extensively for thermal imaging of micro- and nano-electronic devices with a spatial resolution of 50 nm. This paper presents measurement results of the steady state and dynamic temperature responses of the thermal probes and examines the wear characteristics of the probes. [639]**

***Index Terms*—Batch fabrication, cantilever probes, scanning thermal microscopy, thermal design.**

I. Introduction

QUANTITATIVE thermal imaging with sub-100 nm spatial resolution remains a challenging problem, which once solved will enable the investigation of thermophysical phenomena and properties in micro- and nanodevices and structures. Scanning thermal microscopy (SThM) is capable of qualitatively imaging temperature distributions and thermal properties with spatial resolution in the sub-100 nm regime [1]. The SThM maps surface temperature distribution by raster scanning a sharp temperature-sensing tip across the surface. Usually the tip is mounted on a microcantilever beam such that a constant tip-sample contact force is maintained by the force feedback of an atomic force microscope (AFM). The spatial resolution of SThM is unparalleled compared to other thermal imaging techniques based-on far-field optics, such as infrared [2] and laser [3] reflectance techniques, whose spatial resolutions are diffraction limited to be on the order of wavelength. The superior resolution of SThM has made it attractive for thermally detecting failures in ultralarge scale integrated (ULSI) devices, whose minimum feature sizes are scaling down to below 100 nm, and for measuring thermophysical properties of thin films and nanostructures. Most of the previous work in SThM have reported qualitative temperature mapping. Using SThM for quantitatively measuring temperatures and thermal properties in the sub-100 nm has been difficult. This is partly because of the lack of thermal design and batch fabrication of the temperature-sensing probes.

In the past, SThM probes were usually fabricated individually [4], [5], making the process very time consuming and irreproducible. More importantly, for most probes, lack of thermal design led to probes that produced inaccuracies and artifacts in the thermal measurements [4]. For example, if the tip is made of a high thermal conductivity material such as metal [5] or silicon [6], [7], the temperature-sensing tip could act as a heat sink and change the temperature of the sample. The measured tip temperature is then the result of heat flow from the tip to the sample and could be very different from the actual sample temperature. This seriously affects the temperature accuracy and resolution of the measurement. The spatial resolution is related to the temperature resolution [1] and is also degraded by poor thermal design of the probe.

Recently, several groups have attempted to batch fabricate probes for scanning thermal microscopy [6]–[8]. Two groups fabricated thermal probes using only optical lithography and wafer-stage processing steps [6], [7]. However, the probes were made of silicon and are prone to the aforementioned inaccuracies and artifacts. Silicon nitride thermal probes were also fabricated with a thermocouple junction defined at the tip by electron beam lithography [8]. The low throughput of electron beam lithography prohibits the process for being used for large-volume fabrication.

Most of the probes developed till now are passive probes containing a temperature sensor at the tip end. For true temperature measurement using SThM, Nakabeppu *et al.* [9] recently proposed a so called active thermometry scheme that utilized a thermal feedback system to keep the tip temperature equal to the sample temperature and thus maintain zero heat flux between tip and sample. They demonstrated the scheme using individually fabricated thermocouple wire probes. However, only point measurements were realized because of the large thermal time constant (~ 0.5 s) of the large-size wire probe.

To address the issues discussed above, we attempted to thermally design and batch fabricate passive probes for SThM [10]. The following sections describe the modeling, design, fabrication, and characterization of these probes for scanning thermal microscopy with sub-100 nm spatial resolution.

II. Thermal Design

A heat transfer model was developed to optimize the design for the SThM probes to improve the accuracy of the mea-

Manuscript received November 6, 2000; revised February 28, 2001. This work was supported by DOE (Engineering Division, Basic Engineering Sciences), NSF (Chemical and Transport Systems), DARPA HERETIC program, and IBM Austin Research Laboratory. Subject Editor T. Kenny.

The authors are with the Department of Mechanical Engineering, University of California, Berkeley, CA 94720 USA (e-mail: majumdar@me.berkeley.edu)

Publisher Item Identifier S 1057-7157(01)05549-4.

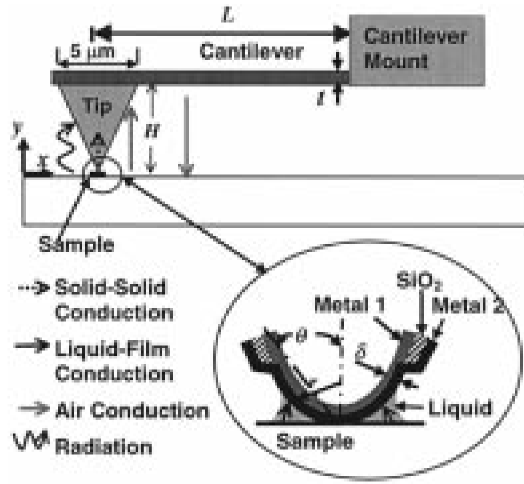

Fig. 1. Schematic diagram of a cantilever probe used for scanning thermal microscopy. The heat transfer mechanisms between the tip, cantilever and the sample are also indicated.

sured temperatures and to reduce heat loss from the sample to the probe. Fig. 1 shows the schematic diagram of a passive probe, which contains a thermocouple junction at the tip end. Tip-sample heat transfer mechanisms include solid-solid conduction through the contact, liquid conduction through a liquid film bridging the tip and sample, air conduction, and radiation [1]. When the measurement was performed near room temperature, radiation heat transfer was estimated to be small compared to the other mechanisms. It was assumed that the temperature was constant at each horizontal cross sections of the tip and only varied along the height or y direction, as shown in Fig. 1. This assumption can be justified because the external thermal resistance through the air is much larger than the internal thermal resistance in the tip across each horizontal cross section. It was further assumed that the sample was a 100 nm diameter nanostructure heated to a temperature T_{s} while the room temperature is T_0. The sample was on a flat substrate with a temperature distribution assumed to be $T_{\mathrm{sub}}(D) = T_0 + (r_{\mathrm{s}}/D)(T_{\mathrm{s}} - T_0)$, which is the solution of the steady state temperature distribution for a point heat source in a uniform medium. Here, $T_{\mathrm{sub}}(D)$ is the temperature of the substrate at a distance D away from the nanostructure, and r_{s} is the radius of the nanostructure. The one-dimensional heat conduction equation in the tip can be written as

$$\frac{d}{dy}\left[(A_{\mathrm{t}}(y)k_{\mathrm{t}}(y) + A_{\mathrm{m}}k_{\mathrm{m}})\frac{dT(y)}{dy}\right] - p(y)h_{\mathrm{a}}(y)\tan\theta(T(y) - T_{\mathrm{sub}}(D)) = 0 \quad (1)$$

where

$$D = r + y\tan\theta. \quad (2)$$

Here, θ and r are the half angle and the radius of the conical tip, respectively, as shown in Fig. 1, A_{t} and k_{t} are the cross-section area and thermal conductivity of the tip, respectively, k_{m} and A_{m} are the cross-section area and thermal conductivity of the metal coating on the tip, respectively, and p is the perimeter of the cross section of the tip. For each point on the perimeter, we assumed that heat was conducted by air between this point and a point right below on the substrate, and treated these two points as two parallel plates. This simplified picture of tip-sample air conduction is represented by the second term in (1), where $T_{\mathrm{sub}}(D)$ is the temperature of the point on the substrate. The distance between the two points on the tip and substrate, respectively, is y. The air conduction coefficient h_{a} needs to be written in different forms for different values of y/λ, where λ is the mean free path of air molecules and is about 60 nm under ambient condition and at sea level [11]. For $y/\lambda > 100$, we assumed a constant temperature gradient at the air gap and used $h_{\mathrm{a}} = \alpha k_{\mathrm{a}}/y$, where k_{a} is the thermal conductivity of bulk air and α is a geometry factor to accommodate the fact that the tip and the substrate is not exactly two parallel plates. We will obtain α by fitting the modeling results with measurement data. For $1 < y/\lambda < 100$, significant temperature discontinuity may develop at the air-solid boundaries because intermolecular collisions become less frequent and molecules arriving at the solid surfaces are unable to come into equilibrium with the surface [11]. In this so-called slip regime

$$h_{\mathrm{a}} = \frac{\left(\frac{\alpha k_{\mathrm{a}}}{y+d}\right)}{\left(\frac{1+2f\lambda}{y+d}\right)}; \quad f = \frac{2(2-A)\gamma}{A(\gamma+1)\mathrm{Pr}} \quad (3)$$

where

- A thermal accommodation coefficient and is about 0.9 for air;
- γ ratio of air heat capacity;
- Pr Prandtl number.

For $y/\lambda < 1$,

$$h_{\mathrm{a}} = \frac{\alpha k'_{\mathrm{a}}}{(y+d)(1+2f)}; \quad k'_{\mathrm{a}} = \frac{CV(y+d)}{3} \quad (4)$$

where k'_{a} is the thermal conductivity of air in the free molecule flow regime, and C and V are the heat capacity and velocity of air molecules, respectively.

The boundary conditions are

$$(A_[\mathrm{t}k_{\mathrm{t}} + A_{\mathrm{m}}k_{\mathrm{m}})\frac{dT}{dy} = \frac{T - T_{\mathrm{s}}}{R_{\mathrm{ts}}}, \text{ at } y = 0 \quad (5a)$$

$$(A_{\mathrm{t}}k_{\mathrm{t}} + A_{\mathrm{m}}k_{\mathrm{m}})\frac{dT}{dy} = \frac{T_0 - T}{R_{\mathrm{c}}}, \text{ at } y = H \quad (5b)$$

where R_{ts} is the tip-sample thermal resistance due to solid–solid and liquid film conduction and will be obtained by fitting the modeling results with measurement data.

The substrate right below the cantilever arm is more than 2.5 μm away from the 100 nm diameter nanostructure, because the base of the tip is usually 5 μm wide, as shown in Fig. 1. At this distance from the nanostructure, the substrate temperatures have decayed significantly from T_{s} and approached room temperature T_0. Accounting for air conduction between the cantilever and the room temperature substrate below, the thermal resistance of the cantilever, R_{c} is solved using fin theory [12]

$$R_{\mathrm{c}} = \frac{\tan h(mL)}{mk_{\mathrm{c}}wt}; \quad m = \sqrt{\frac{h_{\mathrm{a}}}{k_{\mathrm{c}}t}} \quad (6)$$

where $L, w, t,$ and k_{c} are the length, width, thickness, and thermal conductivity of the cantilever, respectively, h_{a} is the

TABLE I
THERMOPHYSICAL PROPERTIES OF CANDIDATE PROBE MATERIALS

	Thermal Conductivity at 300 K (W/m-K) (ref. 13)	Seebeck Coefficient at 300 K (μV/K) (ref 14)
Al	237	-1.66
Au	317	1.94
Cr	93.7	21.8
Ir	147	0.86
Ni	90.7	-19.5
Pt	71.6	-5.28
Ti	21.9	9.1
Si	148	-
SiO_2	1.4	-
SiN_x	5.5 (ref. 15)	-

heat conduction coefficient of the air gap between the cantilever and the substrate and was calculated following the discussion in the preceding paragraph with $\alpha = 1$ because the cantilever and the substrate can be treated as two parallel plates.

The thermophysical properties of candidate probe materials are tabulated in Table I, where the thermal conductivity data of the metals are for pure bulk metals. For the thin film Pt–Cr thermocouple junction probes discussed in the following sections, the thickness of each metal film was measured by AFM to be 75 nm on the cantilever and 25 nm on the tip. To determine the thermal conductivities of the thin metal films, we measured their electrical conductivities as a function of thickness, as shown in Fig. 2. Using Wiedemann-Franz law and assuming that the reduced thermal conductivities of the thin metal films had the same proportionality with the reduced electrical conductivities [16], we estimated the thermal conductivities of the thin metal films. From the electrical conductivity measurements, the correction factors for 75 nm thick films with respect to bulk values were 0.3 for Pt and 0.39 for Cr. For 25 nm thick films, the correction factor were 0.22 for Pt and 0.28 for Cr. For a thermal probe with SiO_2 tip, it is unnecessary to correct the thermal conductivity of SiO_2 at the tip end, because the phonon mean free path in amorphous SiO_2 is expected to be shorter than the size of the tip end [17], which was about 20 nm as shown in the next section.

The two fitting parameters in the above model are $R_{\rm ts}$, the tip-sample thermal resistance, and α, the geometric correction factor for air conduction. We have conducted a series of experiments to study the tip-sample heat transfer mechanisms and to obtain $R_{\rm ts}$ and α. The details of the experiments are described in ref. 18. In short, in the experiments, we measured the temperature of the probe tip as a function of the sample temperature with tip in and out of contact with the sample and for different

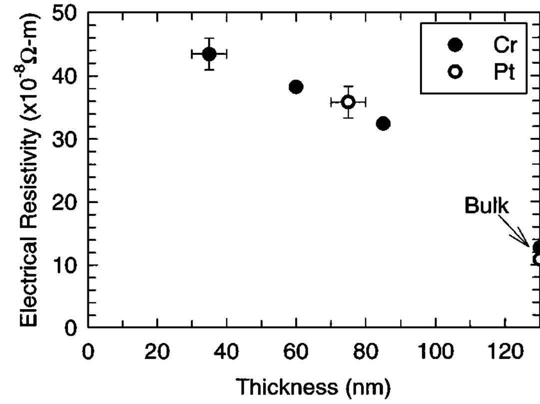

Fig. 2. Electrical resistivity as a function of the thickness of the Pt and Cr films.

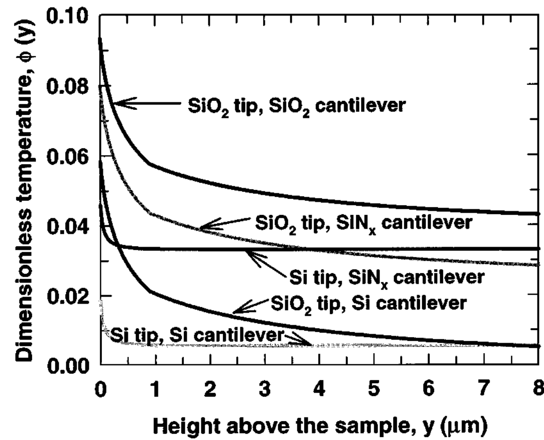

Fig. 3. Temperature distribution in the tip for different tip-cantilever material combination. Cantilever length $L = 150$ μm, width $W = 16$ μm, thickness $t = 0.5$ μm, tip height $H = 8$ μm, tip half cone angle $\theta = 18^\circ$, Cr–Pt junction, thickness of each metal $\delta = 35$ nm, metal linewidth $w = 2$ μm.

contact forces. From the data obtained for the case while tip and sample were out of contact, we determined α to be 0.8 ± 0.1. It is shown by the data that tip-sample solid-solid thermal conductance increased linearly with contact forces for contact force less than 30 nN, and saturated at higher contact forces because of the elastic-plastic contact between an asperity on the tip end and the sample. Form the data, we extracted a tip-sample thermal resistance $R_{\rm ts}$ in the range of $(2.8–4.7) \times 10^7$ K/W for a contact force range of 30–15 nN used in thermal imaging. With these values for $R_{\rm ts}$ and α, the numerical results obtained from the above model fitted well with the measurement results.

With $R_{\rm ts} = 2.8 \times 10^7$ K/W and $\alpha = 0.8$, we solved (1) using a finite difference method to obtain the temperature distribution in the tip, i.e., $T(y)$. A nondimensional temperature of the tip at a distance y away from the sample was defined as

$$\phi(y) = \frac{T(y) - T_0}{T_{\rm s} - T_0} \tag{7}$$

and is plotted in Fig. 3 as a function of y for different tip and cantilever materials. Although the modeling results depended on the value used for $R_{\rm ts}$, the qualitative trend shown in Fig. 3 remains the same as $R_{\rm ts}$ was varied between 10^5–10^8 K/W. Note that if silicon is used as the tip and cantilever materials,

the calculated tip temperature is only a small fraction of the sample temperature. If low-thermal conductivity materials such as SiO_2 and SiN_x are used, the temperature at the tip end can be improved by a factor of about 4. This improvement can increase the temperature response of the thermocouple junction, which is defined as $\phi_j \equiv (T_j - T_0)/(T_s - T_0)$, where T_j is the area-average temperature at the thermocouple junction and was calculated from

$$T_j = \frac{\int_0^h 2\pi x T(y) dy}{\int_0^h 2\pi x dy}; \quad x = r + y \tan\theta \tag{8}$$

where h is the height of the junction and was assumed to be 900 nm.

The spatial resolution Δx is related to temperature response ϕ_j as

$$\Delta x = \frac{\Delta T_{\text{noise}}}{\phi_j \left(\frac{dT_s}{dx}\right)} \tag{9}$$

where ΔT_{noise} is the thermal noise in the thermocouple junction, and dT_s/dx is the temperature gradient on the sample. Equation (9) indicates that the spatial resolution is improved for a larger ϕ_j. Therefore, the spatial resolution will be improved for cantilevers and tips made of SiO_2 and SiN_x.

Attention should be paid in choosing the two dissimilar metals constituting the thermocouple. According to the model, the temperature at the tip end for an Au–Cr thermocouple is about 30% lower than that for a Pt–Cr one because the thermal conductivity of Au is about three times higher than those of Pt and Cr, as shown in Table I. In addition, it is desirable to minimize the metal line widths and film thickness in order to increase the thermal resistances of the tip and cantilever. Another consideration relates to processing. Previous work [4] showed that one of the metals needed to be a noble metal that is resistive to oxidation. The purpose is to achieve low junction electrical resistance R_j because the Johnson noise in the thermoelectric voltage is proportional to $R_j^{0.5}$. Following this, we first chose Pt and Cr and most of the experiments have been performed using probes with Pt–Cr junction. Recently, we have been able to build low electrical resistance junction with nonnoble metals with larger difference in Seebeck coefficients, such as Ni–Cr. This has increased the sensitivity of the probes.

The geometrical parameters of the cantilever, such as cantilever length, width, and thickness, affect the temperature response of the probe, as shown in Fig. 4. The temperature response does not increase much as cantilever length increase more than 100 μm. The reason is that the thermal resistance of the cantilever does not increase further because the cantilever temperature decreases substantially at around 100 μm away from the tip due to air conduction. If the cantilever width is decreased, both heat loss through air conduction and solid conduction can be reduced, resulting in higher temperature response for cantilevers narrower than 10 μm. As shown in Fig. 4, the temperature response also decreases with increasing cantilever thickness due to decreased solid conduction through the cantilever.

The geometric parameters of the tip, such as the tip height and angle, and the junction height also affect the temperature

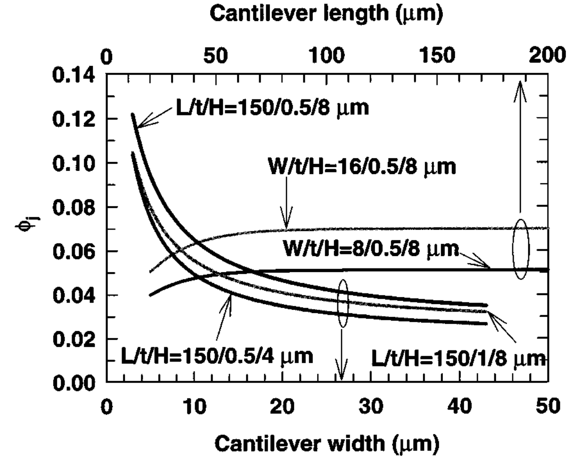

Fig. 4. Dimensionless junction temperature, or temperature response, as a function of cantilever width W (bottom x axis) and length L (top x axis) for different cantilever thickness t and tip height H. SiO_2 tip, SiN_x cantilever, tip half cone angle $\theta = 18°$, Pt–Cr junction, junction height $h = 900$ nm, thickness of each metal film $\delta = 35$ nm, metal linewidth $w = 2$ μm.

response of the probes. Higher tips can reduce air conduction between the cantilever and the substrate and improve the temperature response, as indicated in Fig. 4. A smaller tip angle, or θ in Fig. 1, results in higher thermal resistance in the tip and thus higher temperature at the tip end. In addition, a smaller junction at the very end of the tip will have a higher temperature response, as indicated by Fig. 3.

III. Batch Fabrication Process

According to the above design considerations, we developed a batch fabrication process for making passive thermal probes with SiO_2 tip, SiN_x cantilevers, and a Pt–Cr, Ir–Cr, or Cr–Ni thermocouple junction at the end of the tip. We attempted to minimize the cantilever width, metal line width and thickness, and junction size, and to increase the tip height.

The fabrication process consisted of only wafer-stage processing steps as shown in Fig. 5, with more than 300 probes fabricated on one single wafer. First, a 0.7 μm thick low-pressure chemical vapor deposited (LPCVD) SiN_x film was grown on both sides of 100 mm diameter double-side polished silicon wafers with (100) orientation, followed by the growth of a 8-μm-thick LPCVD silicon dioxide or low temperature oxide (LTO) film. The LTO film on the backside was stripped in buffered HF (BHF 5:1) [Fig. 5(a)]. The LTO on the front side of the wafers was then annealed at 1000°C for one hour. The backside SiN_x was then patterned for use as a mask in a subsequent bulk micro-machining step.

The probe tips were fabricated out of the 8-μm-thick LTO film by reactive-ion-etching (RIE) and wet etching. A chrome film was sputtered on the LTO, and patterned by photoresist into squares [Fig. 5(b)]. Masked by the photoresist and chrome squares, the top 5-μm-thick LTO was etched in CF_4 and CHF_3 plasma. The photoresist plus chrome masks were undercut and the precursor of a sharp-angle tip shape was defined during this etching step. After the RIE etching, the remaining LTO film was etched in BHF 5:1 until the masks were just etched free [see Fig. 5(c)]. Before that, the 8-μm-thick LTO film at the unpro-

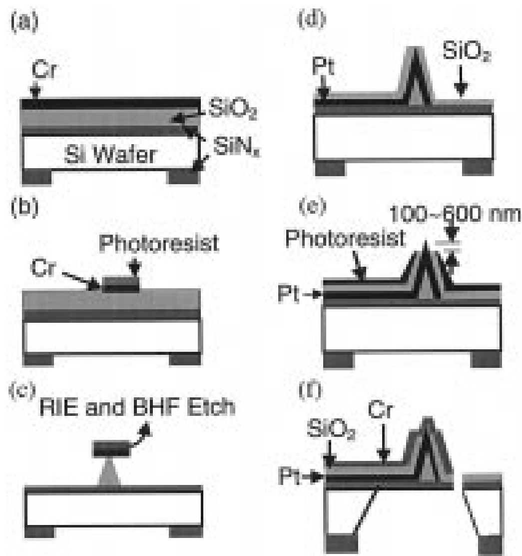

Fig. 5. Fabrication Process. (a) Deposit SiN_x and then SiO_2 by LPCVD, strip SiO_2 and pattern SiN_x at the backside of the wafer, sputter Cr; (b) pattern Cr into 10 μm by 10 μm squares; (c) etch SiO_2 by RIE and BHF until the photoresist and Cr mask was etched free, resulting in a SiO_2 tip; (d) sputter and pattern Pt on the wafer, grow SiO_2 on Pt by LPCVD; (e) spin photoresist on the tip, leaving the tip end uncovered, etch SiO_2 from the tip end; and (f) sputter and pattern Cr on the wafer, pattern SiN_x on the front side of the cantilever, release the cantilever in TMAH.

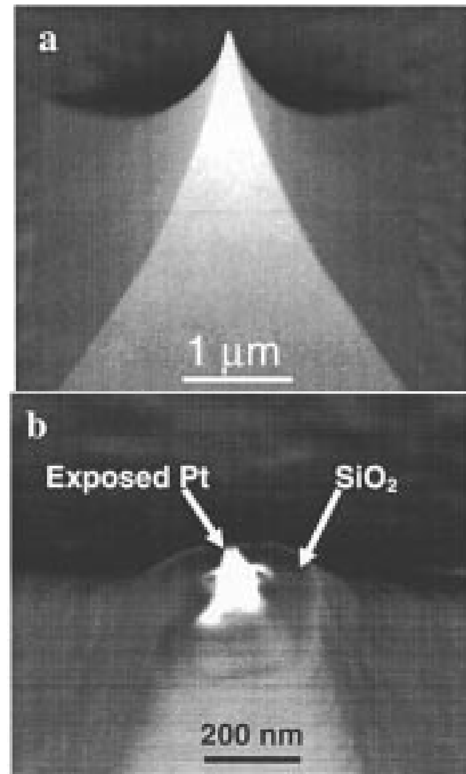

Fig. 6. Scanning electron micrographs of an etched LTO tip (a) after step (c) in Fig. 5 and the detail at the tip end (b) after step (e) in Fig. 5.

tected region etched away. The scanning electron micrographs of an 8-μm tall etched SiO_2 tip is shown in Fig. 6(a). The RIE plus wet etching process could reproducibly yield oxide tips with tip radii about 20 nm and half angles of 10°–20°. Although the BHF step is a critical time etching step, we found that over etching in BHF up to 0.5 μm did not degrade the tip radius. We suspected that some Cr atoms were sputtered into the surface of the LTO film and stayed at the tip end while the photoresist plus Cr masks were just etched free. These Cr atoms might reduce the etching rate of LTO in BHF from the tip end, preventing rounding of the sharp tip.

After the oxide tips were fabricated, a $\sim$ 50-nm-thick platinum film (or chrome film) was sputter deposited and patterned on the front sides of the wafers [see Fig. 5(d)]. A 300-nm-thick LTO was then deposited to cover the tip. Photoresist with appropriate viscosity was spun on the wafer. At a certain spinning speed, surface tension prevents a sharp tip from being covered by a spin-coated photoresist [19], leaving the very ends of the tips uncovered [see Fig. 5(e)]. The LTO film was then etched in BHF 5:1. The height of the etched region depends on the photoresist viscosity and coating speed as well as etching time. We tested several photoresists and chose OCG 825 G-line photoresist. For one 30-s coat of this photoresist at a coating speed of 2000 rpm followed by another 30-s coat at 5000 rpm, the height of the etched region could be made as small as 100 nm high, as shown in Fig. 6(b). However, the yield was only about 30%. While increasing the coating speed of the first coat to 5000 rpm, we found that the junction height increased to about 600 nm high and the yield approached 100%.

After the platinum (or chrome) was exposed at the tip end, the photoresist was stripped and 50-nm-thick chrome (or nickel) was sputter deposited and patterned to form Pt–Cr (or Cr–Ni) junctions [see Fig. 5(f)]. For making Cr–Ni junction, a short sputter etch step was necessary in order to etch the chrome oxide before Ni deposition. After the thermocouples were made, the silicon nitride film was patterned into cantilever shapes. Then 5% tetramethylammonium hydroxide (TMAH) in water was used to etch grooves from the backside of the wafer until the wafer was etched through and the cantilevers were released [see Fig. 5(f)].

Fig. 7 shows two scanning electron micrographs of a finished cantilever probe with the tip containing a Cr–Pt thermocouple junction. The silicon nitride cantilever was designed to be V-shape, with one metal line on each arm. A laser reflector was fabricated between the two arms of the nitride cantilever near the end of the tip. Although the addition of the laser reflector had an equivalent effect of increasing the cantilever width and could degrade the thermal performance of the thermal probes, the reflector was necessary because our AFMs from Digital Instrument used an optical method to detect cantilever deflection. If the laser spot was placed on top of the tip, the tip temperature could rise up to 80 K above ambient. While the laser spot was moved away from the tip to the reflector, tip temperature rise due to laser heating could be reduced to as small as 3 K.

IV. Characterization

The thermal probes have been used for measuring temperature distribution of VLSI via structures [20] and for studying dissipation in multiwall (MW) and single-wall (SW) carbon nanotube (CN) circuits [21]. Fig. 8 shows a topographic and thermal

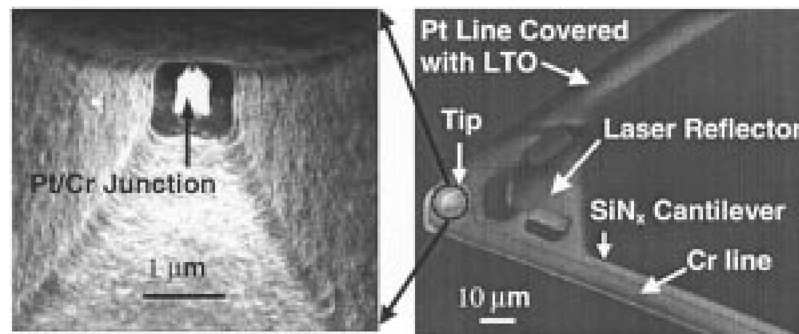

Fig. 7. Scanning electron micrographs of a batch-fabricated probe. Left: Close-up of the Pt–Cr junction at the tip end. Right: Overview of the probe.

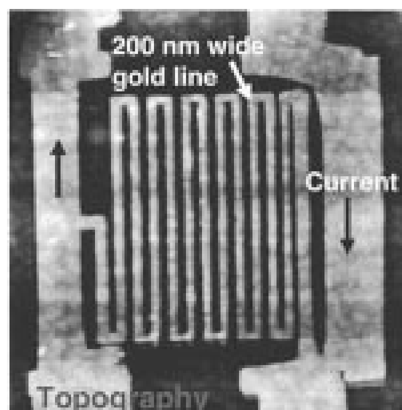

(a)

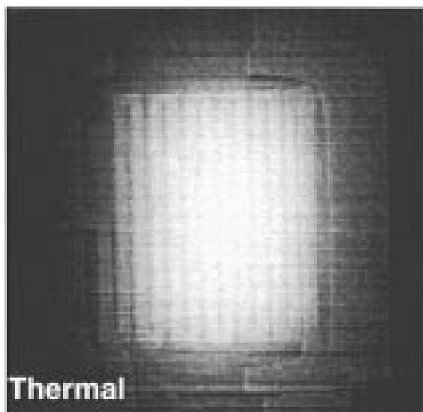

(b)

Fig. 8. Topographic and thermal image of a Joule heated 200-nm-wide gold coil on a oxidized silicon wafer.

image simultaneously obtained by one of the batch-fabricated thermal probes. The sample was a joule heated thin film gold heater coil fabricated by e-beam lithography. The heater line was about 200 nm wide and could be clearly identified in both topographic and thermal images. Fig. 9 shows a topographic and thermal image of a Joule heated MWCN circuit. The temperature profile across the nanotube shows a full-width at half maximum (FWHM) of 50 nm, which demonstrates the spatial resolution of the thermal probe. For both thermal images, a low scan rate of 0.1 Hz, or 0.1 scan line/s, was used in order to suppress the noise in the thermal image. In addition, for imaging the CN circuits, low tip-sample contact forces in the range of 10–20 nN was applied to avoid disturbing electron flow in the nan-

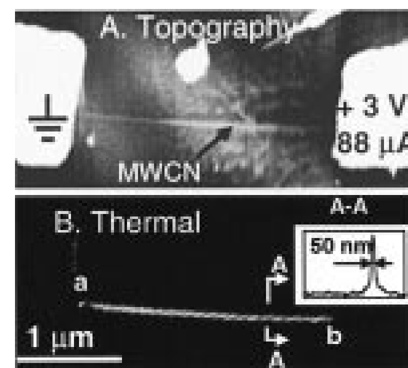

Fig. 9. (A) Topographic and (B) thermal image of a multi wall carbon nanotube (MWCN) circuit. A current of 88 μA passed through the MWCN. The insect in B shows that the FWHM of the temperature profile across the A-A cross section is 50 nm.

otubes or mechanically destroying the sample. Several thermal images at the same contact force were usually obtained for one current flow condition and the temperature profiles from these measurements were consistent with each other. This indicates that tip-sample thermal coupling is stable and constant during the imaging.

The thermal probes were characterized in the following way. First, the thermoelectric power of the Pt–Cr junction was measured to be 13.4 μV/K [20], which is about half of that of a pure bulk Pt–Cr junction. The temperature responses of thermal probes with different geometric parameters were measured using different calibration samples. The calibration samples were thin film aluminum heater lines with different line widths on oxidized silicon wafers. As shown in Fig. 10 as an example, the junction temperatures of the thermal probes in contact with a Joule heated Al line increased linearly with the Al line temperature, which was determined by measuring its temperature-dependant four-probe electric resistance [20]. The temperature responses for different probes on aluminum lines with different line widths are shown in Table II, all on the order of 0.5 K/K. As predicted by the model, the length of the cantilever did not show obvious effect on the temperature response when $L > 100$ μm. The temperature response also showed no obvious dependence on the width as shown in Table II. It should be noted that in Table II, the width of the cantilever was the total width of the two arms of the V-shape cantilever and did not include the laser reflector, which had an area of about 500 μm^2 for all of the probes. Considering the

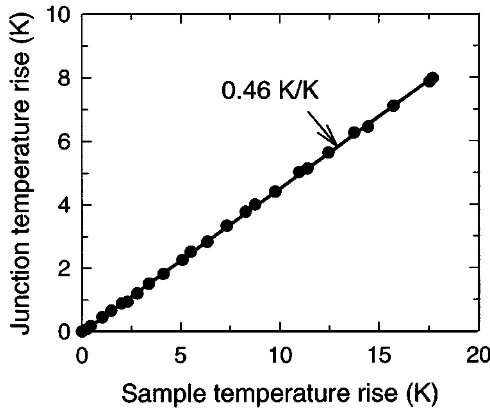

Fig. 10. Junction temperature rise as a function of sample temperature rise. Cantilever length $L = 200$ μm, width $W = 2 \times 8$ μm, thickness $t = 0.7$ μm, Pt–Cr junction height $h = 900$ nm, thickness of each metal $\delta = 50$ nm, metal linewidth $w = 5$ μm. The sample was a Joule heated 3 μm wide, 2000 μm long Al line.

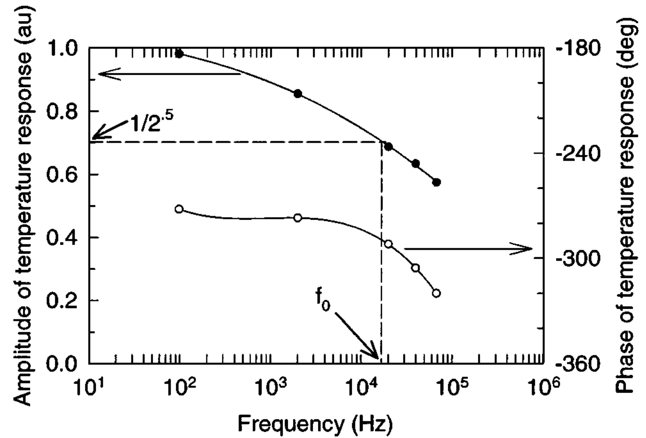

Fig. 11. Dynamic temperature response of the junction as a function of heating frequency.

TABLE II
TEMPERATURE RESPONSE, ϕ_j, OF THERMAL PROBES WITH DIFFERENT DIMENSIONS ON DIFFERENT SAMPLES. L IS THE LENGTH OF THE CANTILEVER. W IS THE WIDTH OF THE CANTILEVER AND IS EXPRESSED AS TWO TIMES THE WIDTH OF EACH OF THE TWO SiN_x ARMS. CANTILEVER THICKNESS $t = 0.7$ μm, TIP HEIGHT $H = 8$ μm, PT–CR JUNCTION, JUNCTION HEIGHT $h = 900$ nm, THICKNESS OF EACH Metal $= 75$ nm, METAL LINEWIDTH $w = 5$ μm. THE CALIBRATION SAMPLES WERE 2000-μm LONG JOULE–HEATED THIN FILM Al LINES WITH DIFFERENT LINEWIDTHS

Sample Linewidth / Probe Dimension	3 µm	5 µm	50 µm
L = 100 µm, W = 2 x 8 µm		0.50±0.05	0.56±0.05
L = 100 µm, W = 2 x18 µm		0.50±0.05	
L = 200 µm, W = 2 x 8 µm	0.46±0.05		0.53±0.05

laser reflector, the effective cantilever width for all the probes in Table II would be much larger than 20 μm. As shown in Fig. 4, the cantilever width should be reduced below 10 μm in order to achieve much higher temperature response. The width of the aluminum line of the calibration sample had a noticeable effect on the temperature response. As the line width increased from 3 μm to 50 μm, the temperature response increased by 0.07 K/K, probably because of the change in air conduction between the cantilever/laser reflector and the substrate. A more in-depth study of tip-sample heat transfer has been performed and is again presented in [18]. In summary, the work found that air conduction depends on the size of the heated region on the sample. For large heated region such as Al lines used here, air conduction is the dominant heat transfer mechanism. For micro/nano devices with submicron heated region, such as a CN circuit or a defective ULSI via structure, air conduction contribution decreases and conduction through the solid-solid contact and the liquid bridge becomes important, giving rise to the sub 100 nm spatial resolution found in the thermal images.

The time constant of the passive probe was measured using a 10-μm-long, 250-nm-wide gold line on an oxidized silicon wafer. A sinusoidal current with a frequency of f was passed through the gold line, resulting in a modulated temperature of the gold line at a frequency of $2f$. The temperature oscillation led to a $2f$ oscillation in the four-probe electrical resistance of the gold line, which was measured and used to calculate the $2f$ temperature. The amplitude and phase of the $2f$ component of the temperature at the Pt–Cr junction was measured by lock-in technique while the probe contacted the gold line. The result is shown in Fig. 11. The AC temperature showed a typical first order dynamic response of $T_{\rm ac} = T_{\rm dc}/\sqrt{1+(2\pi f\tau)^2}$ and decreased to about $1/\sqrt{2}$ at a heating frequency of $f_0 = 18$ kHz. The time constant τ, defined as $1/2\pi f_0$, was calculated to be

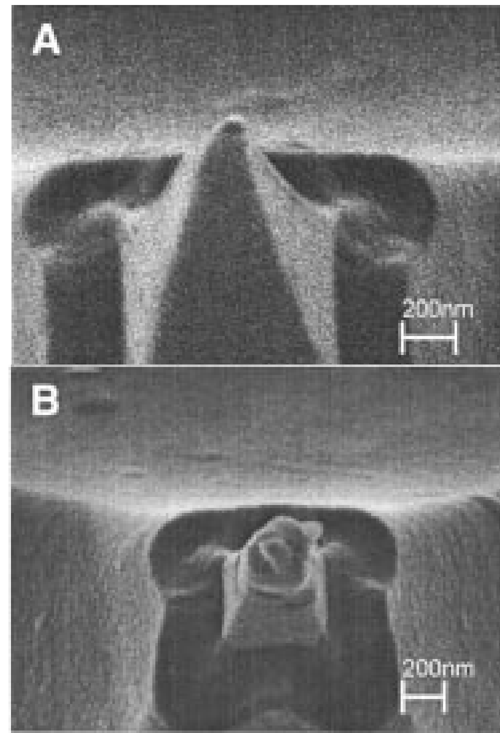

Fig. 12. Scanning electron micrograph of two used thermal probe tips. Tip A showed no wear after obtaining about 10 thermal images of a Joule heated metal lines at contact forces lower than 30 nN. Tip B showed wear at the tip end after scanning over different samples for more than 100 images at contact forces up to 200 nN.

8.8 μs. Previous work [4] measured the time constant of the individually fabricated thin-film thermocouple probes by modulated laser heating. The measured time constant was 0.15 ± 0.02 ms, one order of magnitude larger than that obtained by the current method, which probes the true time constant of a probe measuring temperature of a solid sample.

The wear characteristics of the probe tip was also examined. Fig. 12 shows the SEM images of two used probes after different usage time at different contact forces. Probe A was used to obtain about 10 thermal images of a Joule heated metal lines with tip-sample contact forces less than 30 nN. No noticeable wear was found for this probe. Probe B was used to scan over different samples for more than 100 images at contact forces as large as 200 nN until the sharpness in the topographic image was found to degrade. The SEM image reveals that the tip end was worn, resulting in a broad tip with diameter about 200 nm. To prevent tip wear, during thermal imaging we usually controlled the tip-sample contact force within 30 nN and the tips may last for a few days of experiments without noticeable degrade of the spatial resolution in both topographic and thermal images.

V. Conclusion

We have developed a batch fabrication process for making thermally designed SThM probes for thermal imaging in the sub-100 nm. Based on a heat transfer model, we designed thermal probes with $\mathrm{SiN_x}$ cantilever and $\mathrm{SiO_2}$ tip that can improve sensitivity and spatial resolution in thermal imaging. A RIE and wet etching process was developed to fabricate $\mathrm{SiO_2}$ tips with tip radius of about 20 nm. A thin-film thermocouple junction was made at the end of the $\mathrm{SiO_2}$ tip with a junction height that could be controlled in the range of 100–600 nm. The fabrication process consists of only wafer-stage processing steps with more than 300 probes made on one single wafer. The thermal probes have been used extensively for imaging temperature distribution of micro/nano electronic devices. While the 2–50-μm-wide Joule-heated thin film metal lines were used to calibrate the probes, the temperature responses of the probes were about 0.5 K/K and were influenced by air conduction between the cantilevers and the samples. A more in-depth study of steady-state tip-sample heat transfer mechanisms has been performed and is discussed in [18]. Here, we examined the dynamic response of the probe and measured the thermal time constant of a thermal probe to be 8.8 μs. In addition, the wear characteristics of the thermal probe was investigated and the results show that for low contact forces in the range of 10–30 nN, the thermal probes were not subject to obvious wear for a usage time of a few days.

Acknowledgment

The authors want to thank G. Wu, S. Huxtable, and K. L. Tan for generous assistance during different stages of this work. The thermal image of the carbon nanotube was one of the results from our collaborated project with S. Plyosunov, Dr. P. Kim and Dr.A. Bachtold in Prof. McEuen's group at Department of Physics of University of California, Berkeley. The probes were fabricated in the Microlab of University of California, Berkeley. Our work has been benefited from discussions with Dr. U. Ghoshal from IBM Austin Research Laboratory.

References

[1] A. Majumdar, "Scanning thermal microscopy," *Annu. Rev. Mater. Sci.*, vol. 29, pp. 505–585, 1999.
[2] N. Khurana and C.-L. Chiang, "Analysis of product hot electron problems by gated emission microscopy," in *IEEE Proc. Int. Reliab. Physics Symp.*, 1986, pp. 189–194.
[3] Y. S. Ju and K. E. Goodson, "Short-time-scale thermal mapping of microdevices using a scanning thermoreflectance technique," *J. Heat Transfer*, vol. 120, no. 2, pp. 306–313, 1998.
[4] K. Luo, Z. Shi, J. Varesi, and A. Majumdar, "Sensor nanofabrication, performance, and conduction mechanisms in scanning thermal microscopy," *J. Vac. Sci. Tech. B*, vol. 15, no. 2, pp. 349–360, 1997.
[5] R. J. Pylkki, P. J. Moyer, and P. E. West, "Scanning near-field optical microscopy and scanning thermal microscopy," *Jpn. J. Appl. Phys.*, vol. 33, pp. 3785–3790, 1994.
[6] T. Leinhos, M. Stopka, and E. Oesterschulze, "Micromachined fabrication of Si cantilevers with Schottky diodes integrated in the tip," *Appl. Phys. A*, vol. 66, no. suppl, pp. S65–69, 1998.
[7] Y. Zhang, Y. Zhang, J. Blaser, T. S. Sriram, A. Enver, and R. B. Marcus, "A thermal microprobe fabricated with wafer-stage processing," *Rev. Sci. Instrum.*, vol. 69, no. 5, pp. 2081–2084, 1998.
[8] G. Mills, H. Zhou, A. Midha, L. Donaldson, and J. M. R. Weaver, "Scanning thermal microscopy using batch fabricated thermocouple probes," *Appl. Phys. Lett.*, vol. 72, no. 22, pp. 2900–2902, 1998.
[9] O. Nakabeppu, M. Igeta, and T. Inoue, "Microscale real temperature measurement by the AFM using thermal feedback method," *Thermal Sci. Eng.*, vol. 7, no. 6, pp. 1–7, 1999.
[10] L. Shi, O. Kwon, G. Wu, and A. Majumdar, "Thermal design and batch fabrication of cantilever probes for scanning thermal microscopy," *ASME Int. Mech. Eng. Congress & Exposition, MEMS*, vol. 1, pp. 93–99, 1999.
[11] W. Rohsenow and H. Choi, *Heat, Mass, and Momentum Transfer*. Englewood Cliffs, NJ: Prentice-Hall, 1961.
[12] A. Bejan, *Heat Transfer*. New York: Wiley, 1993.
[13] Y. S. Touloukian and C. Y. Ho, *Thermophysical Properties of Matter*. New York: Plenum, 1972, vol. 1 and 2.
[14] D. M. Rowe, *CRC Handbook of Thermoelectrics*. Boca Raton, FL: CRC, 1995.
[15] The thermal conductivity of low stress $\mathrm{SiN_x}$ was measured by S. Huxtable in our group using the $3 - \omega$ method.
[16] C.-L. Tien, B. F. Armaly, and P. S. Jagannathan, "Thermal conductivity of thin metallic films and wires at cryogenic temperatures," in *Thermal Conductivity*. New York: Plenum, 1969, pp. 13–19.
[17] C.-L. Tien, A. Majumdar, and F. M. Gerner, *Microscale Energy Transport*. Washington, DC: Taylor & Francis, 1998.
[18] L. Shi and A. Majumdar, "Thermal transport mechanisms at nanoscale point contacts," J. Heat Transfer., to be published.
[19] R. C. Davis, C. C. Williams, and P. Neuzil, "Micromachined submicrometer photodiode for scanning probe microscopy," *Appl. Phys. Lett.*, vol. 66, no. 18, pp. 2309–2311, 1995.
[20] L. Shi, O. Kwon, G. Wu, and A. Majumdar, "Quantitative thermal probing of devices at sub-100 nm resolution," in *IEEE Proc. Int. Reliab. Physics Symp.*, 2000, pp. 394–398.
[21] L. Shi, S. Plyasunov, A. Bachtold, P. L. McEuen, and A. Majumdar, "Scanning thermal microscopy of carbon nanotubes using batch fabricated probes," *Appl. Phys. Lett.*, vol. 77, no. 26, pp. 4295–4297, 2000.

Li Shi received the B.E. degree in thermal engineering from Tsinghua University, Beijing, China, in 1991, the M.S. degree in mechanical engineering from Arizona State University, Tempe, in 1997, and the Ph.D. degree in Mechanical engineering from University of California, Berkeley, in 2001.

Between 1991 and 1995, he held a position as an engineer in Guangdong Electrical Power Test and Research Institute in China. He is currently a research staff member of IBM Research Division. His research interests include MEMS, nanotechnology, and thermoelectrics.

Ohmyoung Kwon received the B.S. and M.S. degrees in mechanical engineering from Seoul Nation University, Seoul, Korea, in 1990 and 1992, respectively, and the Ph.D. degree in mechanical engineering from University of California, Berkeley, in 2000.

He is currently a Postdoctoral Researcher of the Berkeley Sensor and Actuator Center at the University of California, Berkeley. His research interests include design, fabrication, micro/nanoscale thermal imaging and nondestructive evaluation of MEMS and microelectronic structures.

Andrew C. Miner received the B.S.E. degree in mechanical engineering from Arizona State University (Main Campus), Tempe, in 1997, and the M.S. degree in mechanical engineering from the University of California-Berkeley in 1999. He is pursuing the Ph.D. degree in the Nanoengineering lab at the University of California, Berkeley and his research interests include thermoelectrics, MEMS and scanning probe microscopy.

Arunava Majumdar received the B.Tech degree in mechanical engineeringfrom the Indian Institute of Technology, Bombay, in 1985 and the Ph.D. degree in mechanical engineering from University of California, Berkeley, in 1989.

He is currently a Professor and the Vice-Chairman of Instructions in the Department of Mechanical Engineering, University of California, Berkeley. Previously, he was with the Arizona State University, Tempe, from 1989 to 1992 and the University of California, Santa Barbara (from 1992 to 1996 as a faculty member in mechanical engineering. His research interests in his group range from MEMS, micro/nanoscale thermophysics to nanobiomolecular engineering and nanoscale imaging. He is currently serving as an Associate Editor for the *ASME Journal of Heat Transfer* and the *International Journal of Heat and Mass Transfer*, and is Co-Editor-in-Chief of *Microscale Thermophysical Engineering*.

Dr. Majumdar is a recipient of the NSF Young Investigator Award, the ASME Melville Medal, and the ASME Best Paper Award from the Heat Transfer Division. He also serves as a member of the Council on Energy Engineering Research for the Department of Energy and the ASME Steering Committee on Nanotechnology.